Journal of Carbon Research

MDPI

Article

Effect of Synthesis Conditions on the Structure and Electrochemical Properties of Vertically Aligned Graphene/Carbon Nanofiber Hybrids

Mahnoosh Khosravifar [1], Kinshuk Dasgupta [2] and Vesselin Shanov [1,3,*]

[1] Department of Mechanical and Materials Engineering, University of Cincinnati, Cincinnati, OH 45221, USA; khosramh@mail.uc.edu
[2] Materials Group, Bhabha Atomic Research Centre, Mumbai 400085, India; kdg@barc.gov.in
[3] Department of Chemical and Environmental Engineering, University of Cincinnati, Cincinnati, OH 45221, USA
* Correspondence: shanovvn@ucmail.uc.edu

Abstract: In recent years, significant efforts have been dedicated to understanding the growth mechanisms behind the synthesis of vertically aligned nanocarbon structures using plasma-enhanced chemical vapor deposition (PECVD). This study explores how varying synthesis conditions, specifically hydrocarbon flow rate, hydrocarbon type, and plasma power,—affect the microstructure, properties, and electrochemical performance of nitrogen-doped vertically aligned graphene (NVG) and nitrogen-doped vertically aligned carbon nanofibers (NVCNFs) hybrids. It was observed that adjustments in these synthesis parameters led to noticeable changes in the microstructure, with particularly significant alterations when changing the hydrocarbon precursor from acetylene to methane. The electrochemical investigation revealed that the sample synthesized at higher plasma power exhibited enhanced electron transfer kinetics, likely due to the higher density of open edges and nitrogen doping level. This study contributes to better understanding the PECVD process for fabricating nanocarbon materials, particularly for sensor applications.

Keywords: PECVD; vertically aligned graphene; carbon nanofibers

Citation: Khosravifar, M.; Dasgupta, K.; Shanov, V. Effect of Synthesis Conditions on the Structure and Electrochemical Properties of Vertically Aligned Graphene/Carbon Nanofiber Hybrids. *C* **2024**, *10*, 97. https://doi.org/10.3390/c10040097

Academic Editors: Camélia Matei Ghimbeu and Encarnación Raymundo-Piñero

Received: 18 October 2024
Revised: 20 November 2024
Accepted: 21 November 2024
Published: 24 November 2024

1. Introduction

Vertically aligned graphene (VG) and vertically aligned carbon nanofibers (VCNFs) have garnered considerable attention in recent years due to their exceptional structural properties and wide range of potential applications, including sensors, energy storage, and more [1–4]. These materials exhibit remarkable electrical, thermal, and mechanical properties, and the ability to finely tune their microstructure through synthesis conditions is crucial for optimizing their performance for various applications.

The PECVD technique is a widely used method for synthesizing vertically aligned carbon structures [5–8]. PECVD systems typically include a plasma generator, a precursor gas source, and a vacuum heating chamber where deposition occurs. Various plasma sources, such as microwave (MW), radio frequency (RF), and direct current (DC), can be used, each with distinct characteristics that influence the growth of carbon nanostructures. MW-based PECVD generates high electric fields and facilitates uniform growth, while RF systems can operate in inductively or capacitively coupled modes. Inductively coupled plasma (ICP) systems are preferred for their ability to produce high electron density and reactive species, while capacitively coupled plasma (CCP) systems typically require combination with other plasma sources for optimal nanostructure growth. DC plasma, on the other hand, offers a strong electric field and enhanced ion flux, leading to faster growth rates and better alignment of nanostructures, making it particularly effective for large-scale production [9–11].

During the past few years, efforts have been made to understand the growth mechanism of vertically aligned carbon structures synthesized with different plasma sources using the PECVD method [12–18]. Kulczyk-Malecka et al. used the MW-PECVD method for optimizing deposition conditions to enhance the morphology, growth rate, and electrochemical performance of VGs [19]. The low-temperature synthesis of CNFs by RF-PECVD was studied by Wang et al., who explored the growth mechanisms of CNFs and compared the results with traditional thermal CVD methods [20].

In our previous research, a hybrid structure of NVG/NVCNFs was successfully synthesized on an N3DG substrate using the PECVD method [21]. That study explored the growth mechanism of the hybrid structure and related electrochemical performance, highlighting its potential for applications in supercapacitors. The current work extends this investigation by evaluating various synthesis conditions, including hydrocarbon percentage, plasma power, and hydrocarbon type, to assess their effects on the final microstructure and surface properties of the hybrid structure. Factors such as the hydrocarbon nature and concentration, along with the plasma power, were systematically varied, and their impacts on the microstructure were analyzed. Additionally, the electrochemical performance of the obtained hybrids was also compared, and the best-performing sample was studied in terms of its sensitivity towards Pb^{2+} detection. By systematically investigating the selected PECVD variables, we seek to optimize the synthesis process and enhance the performance of synthesized nanostructures for advanced technological applications.

2. Materials and Methods

The catalyst used for the synthesis of NVG)/NVCNFs hybrid structures was prepared by a slurry cast method using a specific mixture of 3–7 µm Ni powder, polystyrene, and diethylene glycol dibenzoate (DEGDB). Then, the dried cast was heated to 1000 °C in argon (Ar) and hydrogen (H_2) for 10 min to anneal the Ni particles and remove the polymer [22,23].

The two-step synthesis of the hybrid structure was carried out in a Black Magic™ (AIXTRON, Herzogenrath, Germany) reactor and is described in detail in our previous publication [21]. In summary, a nitrogen-doped three-dimensional graphene was synthesized by LPCVD as the first structure (which also acts as a substrate for the following synthesis step). In this step, the N3DG was synthesized at 850–900 °C and a gas mixture of 15 sccm methane (CH_4), 300 sccm ammonia (NH_3), and 1175 sccm argon (Ar) for 10 min while holding the pressure at 25 mbar. Then, the process conditions were switched to a PECVD mode to obtain the final structure.

The PECVD step was carried out with varying parameters to correlate the synthesis conditions with the obtained structures. Hydrocarbon flow rate, hydrocarbon type, and plasma power were used as varying factors for the study. Acetylene (C_2H_2) and methane (CH_4) were utilized as hydrocarbon sources, with acetylene flow rate adjusted to study its impact on the growth of the final structure. Additionally, the plasma power was varied to evaluate its effect on the NVG/NVCNFs structure. During the PECVD process, the plasma components were recorded by optical emission spectroscopy (HR 4000 CG-UV-NIR, Ocean Insights, Largo, FL, USA). The details of synthesis conditions are outlined in Table 1.

After the synthesis steps, the final NVG/NVCNFs hybrid structures were acquired by etching the Ni catalyst in a 50% HCl solution.

The obtained nanocarbon materials were studied and compared by employing various characterization techniques. Microstructural analysis was carried out using an Apreo FESEM (ThermoFisher, Waltham, MA, USA). An inVia Raman microscope (Renishaw, Wotton-under-Edge, UK) was used to conduct Raman spectroscopy with 50× objective optical lens, 514 nm laser, output power, and a spot size of 8 mW and 1–5 µm, respectively. X-ray Photoelectron Spectroscopy (XPS) was performed on hybrid structures using a VG Thermo-Scientific ML 3000 UHV (ThermoFisher, Waltham, MA, USA) to identify the amount and type of nitrogen in the material.

Table 1. PECVD conditions for synthesis of the vertical hybrid structure. A and M stand for acetylene and methane, respectively. H stands for hybrid structure. Numbers after AH and MH represent the percentage of hydrocarbon flow/total flow. AH15-160 was prepared with the same synthesis conditions as AH15, except the plasma power was set at 160 W instead of 120 W.

Sample Name	Hydrocarbon Type	Hydrocarbon Flow/Total Flow	Plasma Power	Synthesis Time	Synthesis Temperature
AH15	C_2H_2	15%	120 W	6 min	650 °C
AH7	C_2H_2	7%	120 W	6 min	650 °C
AH15-160	C_2H_2	15%	160 W	6 min	650 °C
MH15	CH_4	15%	120 W	6 min	650 °C

The electrochemical measurements were performed with a Gamry electrochemical workstation (Warminster, PA, USA) using a three-electrode setup with hybrid structures as the working electrode, and silver/silver chloride (Ag/AgCl) and platinum as the reference electrode and counter electrode, respectively. The cyclic voltammetry (CV) was conducted in a 5 mM hexaammineruthenium (III) chloride (Ru $(NH3)^{3+/2+}$ or RuHex) containing 0.5 M KCl electrolyte at scan rates between 5 to 200 mV/s and the potential window of −0.4 V to 0.1 V. Square wave anodic stripping voltammetry (SWASV) was utilized for detection of Pb^{2+} in 0.1 M acetate (NaAc/HAc) buffer solution (PH = 4.5) containing known concentrations of lead ions between 5–35 ppb. The deposition potential was set at −1.2 V for 240 s, and the potential ranges between −1.2 V to 0 V with the amplitude, frequency, and increment potential of 50 mV, 30 Hz, and 10 mV, respectively. A cleaning step was performed before each experiment for 60 S with a desorption potential of 0.5 V for removing the residual metals on the electrode.

3. Results and Discussion

The hybrid structures were synthesized in two steps, with the PECVD run beginning immediately after the LPCVD step. The PECVD conditions, including hydrocarbon flow rate, hydrocarbon type, and plasma power, were changed to achieve four different hybrid structures. The effect of each factor on the final microstructure, properties, and electrochemical performance was studied and compared in this section.

The microstructure of obtained hybrids was evaluated by FESEM after removing the Ni catalyst, as shown in Figure 1. As observed in Figure 1a–c, the top layer of the hybrid structures involves flower-like NVG accompanied by NVCNFs structures where the NVCNFs grow alongside the NVGs. The amount and density of NVGs and NVCNFs varies with the different synthesis conditions mentioned in Table 1.

The growth mechanism for these types of structures was discussed in detail in our previous publication [21]. In summary, an N3DG/Ni structure was synthesized after conducting the LPCVD step, followed by exposure to PECVD for growing the top layer. The growth started with the introduction of the N3DG layer to the reactive plasma species, including plasma etchants (H radicals, NH, and N^{2+}). The latter caused the generation of defects and dangling bonds on the N3DG surface, which acted as nucleation sites for the vertical structures. The NVG/NCNF hybrid grew in the direction of the plasma electric field, resulting in the formation of a vertical top structure perpendicular to the N3DG/Ni substrate.

According to our previous study, the nanosized Ni catalysts for the growth of NVCNFs were supplied during the PECVD process from the Ni present in the N3DG/Ni substrate. Two main sources for nanosized Ni were proposed: (1) formation of semispherical Ni islands on the Ni facets to minimize surface energy, and (2) sputtering and redeposition of Ni nanoparticles caused by the plasma species produced via decomposition of NH_3 and C_2H_2 [24,25].

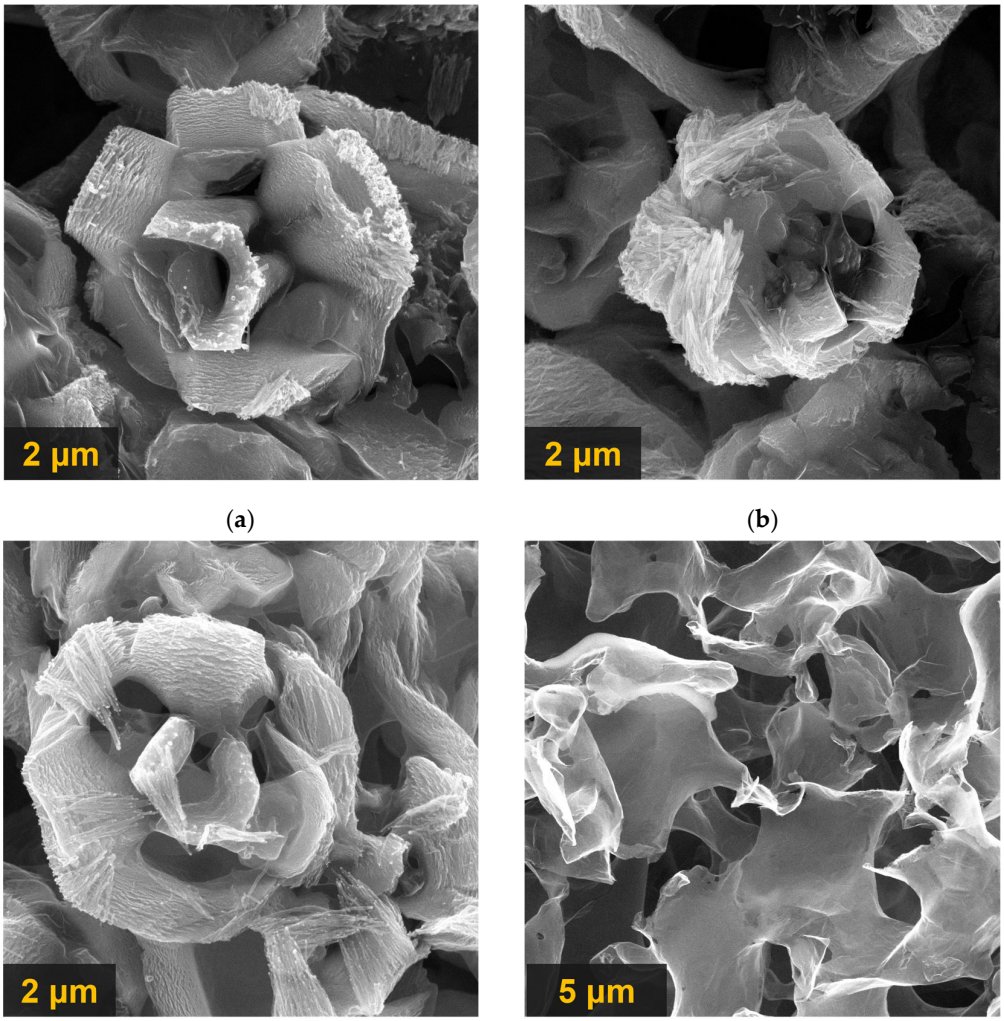

Figure 1. FESEM images of (**a**) AH15; (**b**) AH7; (**c**) AH15-160; and (**d**) MH15. Details about the growth conditions of the imaged samples are given in Table 1.

Figure 1a,b shows the microstructural differences between the two samples with varying acetylene flow rates as per Table 1. The sample with a 15% flow rate (AH15) exhibited well-developed, thicker flower-like NVGs with NVCNFs grown along the NVG walls, while the AH7 sample showed incomplete NVG structures accompanied by NVCNFs outgrown the NVGs along their walls. In AH15, NVGs and NVCNFs appeared to have grown simultaneously alongside each other, indicating that the hydrocarbon concentration can influence the size, height, and shape of the achieved microstructure [26,27]. The incomplete growth of NVGs in AH7 was likely due to an insufficient carbon source resulting from the reduced hydrocarbon feed compared to AH15. Another contributing factor could be the deficient carbon feed on the catalyst surface due to the higher ratio of NH_3/C_2H_2 in AH7, which led to an increased presence of plasma etchants such as hydrogen radicals, NH, and N^{2+} [19]. Such an over-etching of the carbon species on the catalyst surface likely hindered the nucleation and growth of NVGs. It has been reported that the hydrocarbon concentration can also influence the number of graphene layers within the obtained material. Dervishi et al. observed that lower acetylene concentrations resulted in a reduced number of graphene sheets in the final structure [26].

The effect of plasma power on the microstructure of the hybrids was examined by synthesizing samples at two plasma powers of 120 W and 160 W, with the acetylene flow rate/total flow rate maintained at 15% (Figure 1a,c). According to the microstructures in

Figure 1a,c, higher plasma power in the AH15-160 hybrid led to a more compact structure with a greater abundance of NVGs and NVCNFs. This was likely due to the increased ionization caused by the higher plasma power, which generated more carbon species on the catalyst surface, leading to a greater number of nucleation sites. Additionally, the elevated plasma power increased the production of plasma etchants (hydrogen radicals, NH, N^{2+}), which actively removed amorphous carbon from the catalyst surface and further enhanced the growth of carbon structures [28,29]. This observation aligns with the OES results, where the plasma components were recorded at different plasma powers (Figure S1).

When comparing the hybrids obtained using acetylene and methane as hydrocarbon sources, distinct differences in microstructure were observed, as shown in Figure 1a,d. The sample synthesized with acetylene exhibited the characteristic flower-like NVGs and NVCNFs, while the sample with methane did not show these features. This difference can be attributed to the lower decomposition rate of methane compared to acetylene under the same processing conditions. Methane's slower decomposition under similar synthesis conditions led to a porous nitrogen-doped 3D-Graphene (N3DG) structure with many open edges and a slight vertical alignment towards the plasma electric field direction. The NVG/NVCNFs structure seen with acetylene was not achieved with methane due to the limited number of carbon species resulting from the lower decomposition rate of methane under similar synthesis parameters [27].

SEM images of the microstructural comparison for all obtained hybrid samples before Ni catalyst removal are presented in Figure S2a–d. The structural variation with different synthesis conditions was also evident in the samples where Ni was not etched and remained present. In AH7/Ni, the incomplete growth of NVGs was observed, with only NVCNFs developing due to the reduced carbon source and higher etching environment, while AH15/Ni demonstrated a fully formed NVG/NVCNFs hybrid with complete flower-like growth. The AH15-160/Ni sample exhibited NVG/NVCNFs flowers with multiple petal layers, which could be attributed to the increased decomposition rate of the precursor gases, facilitating enhanced growth. In contrast, the MH15/Ni sample revealed a Ni catalyst framework covered by a nitrogen-doped 3D graphene (N3DG) structure, indicating a different growth dynamic compared to the acetylene-based structures.

XPS was employed to analyze the surface chemistry of synthesized hybrid structures, and the results are shown in Figure 2. The XPS data for AH15 were reported previously [21]. The high-resolution C1s spectra of the hybrids are shown in Figure 2a–c, revealing three prominent peaks corresponding to sp^2-C (284.5 eV), N-sp^2-C (285.7 eV), and N-sp^3-C (286.8 eV). The primary peak at 284.5 eV represents the sp^2-hybridized carbon, which is dominant in graphitic structures.

Nitrogen doping within the structures was quantified using the high-resolution N1s spectra (Figure 2b,d,f), with the nitrogen configurations mainly broken down into graphitic N, pyridinic N, and pyrrolic N. The total nitrogen content was found to vary depending on the synthesis conditions. For AH7, AH15-160, and MH15, the nitrogen doping amounts were calculated as 4.2 at%, 5.1 at%, and 1.9 at%, respectively. Previous work reported a nitrogen doping of 4.4 at% for AH15 [21].

The variation in nitrogen doping levels between the hybrid structures can be attributed to differences in the ionization rates of the hydrocarbon and ammonia, along with the availability of bonding sites for nitrogen incorporation. In hybrids synthesized with acetylene, the higher decomposition rate of this precursor provided more carbon species for NVG/NVCNFs growth, increasing the number of active carbon sites for nitrogen bonding. On the other hand, in MH15, the lower decomposition rate of methane resulted in fewer carbon species, limiting bonding opportunities and reducing nitrogen incorporation.

The increased nitrogen doping level in AH15-160 can be linked to the higher plasma power, which enhances the ionization of both acetylene and ammonia, thus generating more active sites, defects, and dangling bonds on the surface of the growing structure and facilitating enhanced nitrogen incorporation into the carbon lattice.

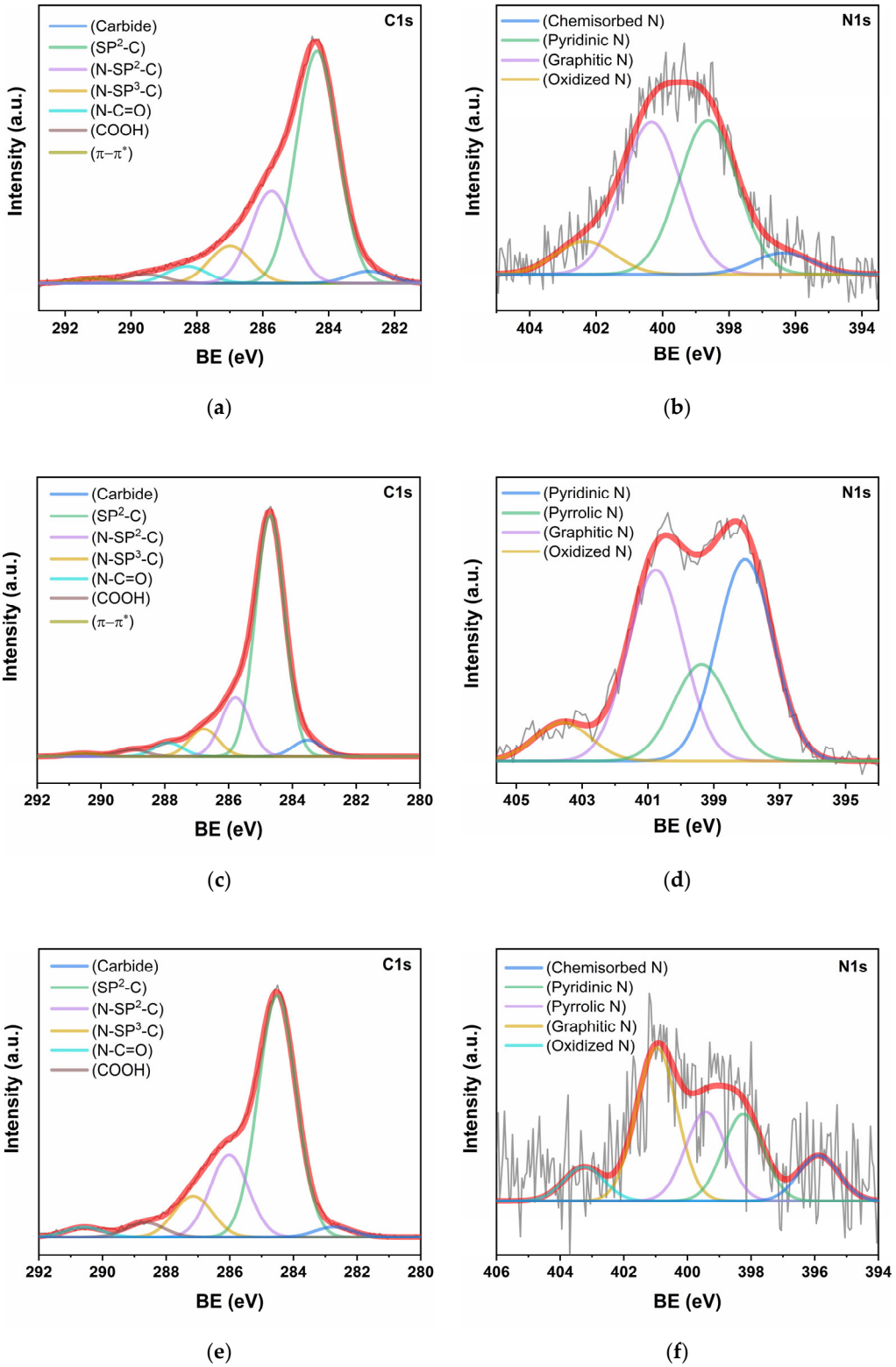

Figure 2. XPS spectrum of C1s for (**a**) AH7, (**c**) AH15-160, and (**e**) MH15; XPS spectrum of N1s for (**b**) AH7, (**d**) AH15-160, and (**f**) MH15. Gray and red lines represent the experimental and fitted curves, respectively.

The N doping level in AH15 and AH7 showed only a marginal difference despite the higher acetylene concentration in AH15. The marginal increase in N doping in AH15 may be due to the greater availability of carbon species, which provided slightly more

bonding sites for nitrogen incorporation. However, the difference is minimal, and the nitrogen incorporation process appeared to be more influenced by the plasma conditions rather than the variations in the hydrocarbon supply. Further analysis of the nitrogen bonding configurations showed that AH7 contained 42% graphitic nitrogen and 42% pyridinic nitrogen, indicating significant nitrogen incorporation at the graphene lattice edges and within its basal planes. For AH15-160, the nitrogen doping consisted of 33% graphitic nitrogen, 36% pyridinic nitrogen, and 17% pyrrolic nitrogen, reflecting two nitrogen configurations primarily at the lattice edges. In comparison, MH15 exhibited lower nitrogen content, with 33% graphitic nitrogen, 18% pyridinic nitrogen, and 19% pyrrolic nitrogen contributing to its overall composition.

The role of nitrogen doping in enhancing electrochemical performance is well-known, as nitrogen can improve conductivity, active surface area, and wettability [30,31]. While the total nitrogen content has been shown to influence this performance, the nitrogen configuration, especially pyridinic and pyrrolic nitrogen, plays a crucial role in improving overall electrochemical behavior.

Raman spectra of the hybrid structures are shown in Figure 3. At a glance, the difference between the spectra of the three acetylene-synthesized and the methane-synthesized samples was apparent. This indicated that the NVG/NVCNFs structures have a characteristic Raman spectrum that reflects the presence of both NVGs and NVCNFs. All samples exhibited three primary bands: the G band, associated with the graphitic structure; the D band, which indicates defects; and the 2D band, characteristic of the graphene structure [19]. In the MH15 sample, the D' peak, seen as a shoulder of the G band, was linked to defects in the graphitic structure directly tied to nitrogen doping.

Due to the coexistence of various graphitic structures and defects in the acetylene-based samples, an exact comparison of their Raman spectra is challenging. Factors such as the number of graphene layers, nitrogen doping levels, and the open edges from NVG and NVCNFs structures likely contribute to the observed spectra. AH15-160 exhibited a higher I_D/I_G ratio of 0.77 compared to AH15 and AH7, which can be attributed to a greater number of defects, primarily due to the increased number of open edges in the NVGs and NVCNFs, along with higher nitrogen doping. Additionally, the high density of NVCNFs, combined with multiple graphene layers and nitrogen doping, could explain the reduced intensity of the 2D peak in comparison to AH15 and AH7 [32,33].

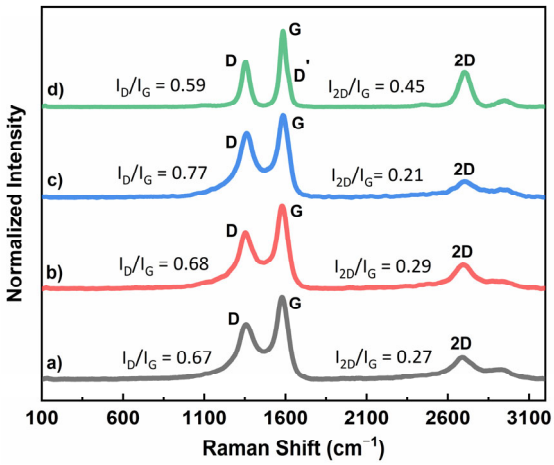

Figure 3. Raman spectrum of (**a**) AH15, (**b**) AH7, (**c**) AH15-160, and (**d**) MH15.

Meanwhile, the Raman spectrum of the MH15 sample showed a typical graphene signature with a high D intensity due to defects, including open edges and nitrogen doping. The D peak intensity in MH15 was lower than in the AH samples, indicating fewer defects.

Electrochemical measurements were conducted to evaluate the electron transfer properties of the hybrid materials using a 5 mM RuHex outer-sphere redox probe containing

0.5 M KCl. The obtained CV results are shown in Figure 4a, where the peak-to-peak separation (ΔE_p) for AH15, AH7, AH15-160, and MH15 were measured as 100 mV, 106 mV, 96 mV, and 120 mV, respectively. The observed peak-to-peak potential values were higher than the 59 mV for a fully reversible reaction, indicating quasi-reversible electron transfer kinetics across all samples [34]. AH15-160 exhibited the lowest ΔE_p, which suggests a faster electron transfer rate. This is attributed to the high density of available open edges from NVG and NVCNFs as well as the higher nitrogen doping content compared to the other samples. The abundance of open edges in the hybrid structures enhances the electrochemical activity by providing active sites for electron transfer, while nitrogen doping, particularly pyridinic and pyrrolic configurations, further facilitates the electron transfer process [35,36].

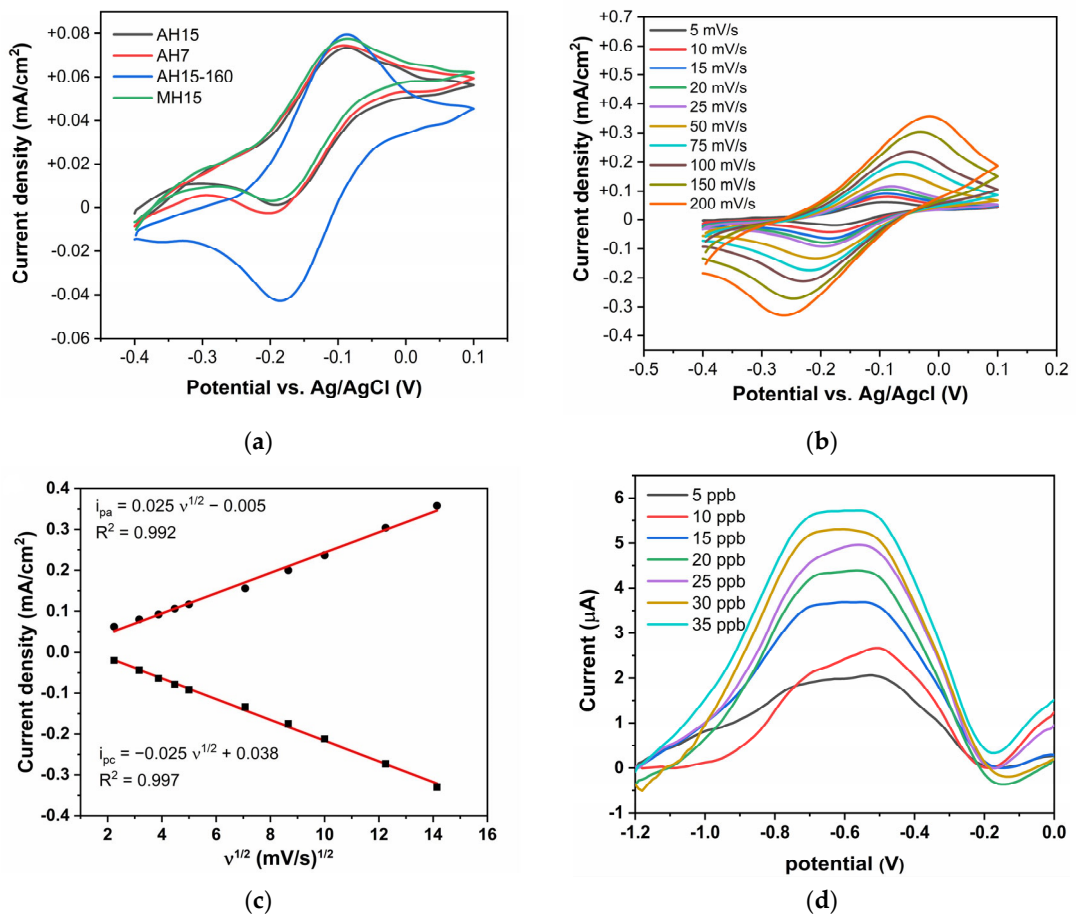

Figure 4. (**a**) CV response of all the hybrid samples in 5 mM RuHex containing 0.5 M KCl at 10 mV/s scan rate, (**b**) CV curves of AH15-160 at scan rates of 5–200 mV/s, (**c**) peak current versus $\nu^{1/2}$ for AH15-160 hybrid where $\nu^{1/2}$ is the square root of the scan rate, i_{pa} and i_{pc} are the peak anodic and cathodic currents, respectively, and (**d**) SWASV response of AH15-160 in 0.1 M acetate buffer solution containing various Pb^{2+} concentrations from 5 ppb to 35 ppb.

The CV response of AH15-160 at scan rates ranging from 5 mV/s to 200 mV/s is shown in Figure 4b, where the peak current increased with higher scan rates. A linear relationship between the peak current and the square root of the scan rates (Figure 4c) indicated that the reaction was diffusion controlled [34].

Due to its enhanced electrochemical performance compared to other hybrid samples, AH15-160 was selected for Pb^{2+} sensing analysis. Square wave anodic stripping voltammetry (SWASV) was used to determine the response of the AH15-160 electrode in 0.1 M acetate buffer solution (PH = 4.5) containing known concentrations of lead ions. In this method, Pb^{2+} ions in solution were reduced to Pb in a pre-concentration step and deposited on the electrode surface with a negative potential, followed by a stripping step where Pb was

re-oxidized to Pb^{2+} under the application of a square-wave potential. The response was recorded between −1.2 V and 0 V as the Pb^{2+} concentration in the solution was increased from 5 ppb to 35 ppb, and the response was recorded and shown in Figure 4c. The SWASV results indicated that AH15-160 is highly sensitive to the presence of Pb^{2+} in the solution, suggesting that it could be a strong candidate for lead sensing applications.

According to the World Health Organization (WHO), the permissible limit of lead in water is below 10 ppb [37]. Based on its performance, the tested AH15-160 electrode demonstrated great sensitivity to Pb^{2+}, thus showing a promising performance for trace-level heavy metal detection down to a few ppb. However, additional studies are needed to evaluate the sensing capabilities of the created electrode, particularly in tap water, where interference from copper ions and other heavy metals may be present.

The encouraging test results of AH15-160 can be attributed to several factors. One is the high nitrogen doping level, specifically the presence of pyrrolic and pyridinic nitrogen, which plays a critical role in Pb^{2+} adsorption. Additionally, the open edges of NVGs and NVCNFs provide accessible pathways for electron transfer, which is crucial for the redox process in Pb^{2+} detection. Overall, the combination of nitrogen doping and the hybrid's unique microstructure significantly contributes to the electrode's sensing capabilities.

4. Conclusions

NVG/NVCNFs hybrid structures were successfully synthesized using a two-step process involving LPCVD followed by PECVD. Four distinct hybrid structures were obtained by adjusting the PECVD parameters, including hydrocarbon flow rate, hydrocarbon type, and plasma power. The effects of varied synthesis conditions on the microstructure, surface properties, and electrochemical performance were studied.

The microstructural analysis revealed that acetylene-based samples with greater hydrocarbon flow rates and plasma powers exhibited more developed NVG and NVCNFs structures, with AH15-160 displaying a denser and more compact microstructure. This was attributed to the increased ionization and carbon species generation, leading to enhanced nucleation and vertical growth of NVGs and NVCNFs. In contrast, the methane-based sample did not form NVG/NVCNFs structures due to the lower decomposition rate of this hydrocarbon compared to acetylene, resulting in a porous N3DG structure.

XPS analysis confirmed the presence of various nitrogen configurations, with pyridinic and pyrrolic nitrogen playing crucial roles in the electrochemical behavior of the hybrid structures. The high I_D/I_G ratio for AH15-160 in Raman, coupled with a reduced 2D peak intensity, indicated a greater number of defects and open edges, which are beneficial for enhancing electrochemical activity.

Electrochemical measurements indicated quasi-reversible electron transfer kinetics for all samples, with AH15-160 revealing better electron transfer efficiency compared to the other tested samples. The high density of open edges and nitrogen doping in AH15-160 contributed to its enhanced performance. SWASV measurement of AH15-160 demonstrated great sensitivity for Pb^{2+}, making this hybrid structure a promising candidate for fabricating electrodes to detect trace-level heavy metals in water.

Supplementary Materials: The following supporting information can be downloaded at: https://www.mdpi.com/article/10.3390/c10040097/s1, Figure S1: Comparison of optical emission spectroscopy data obtained from AH15 and AH15-160; Figure S2. SEM images of (a) AH15, (b) AH7, (c) AH15-160, and (d) MH15 before removing Ni catalyst.

Author Contributions: Conceptualization, M.K., K.D. and V.S.; methodology, M.K. and K.D.; software, M.K.; validation, M.K.; formal analysis, M.K.; investigation, M.K. and V.S.; resources, V.S.; data curation, M.K.; writing—original draft preparation, M.K.; writing—review and editing, M.K., K.D. and V.S.; visualization, M.K.; supervision, V.S.; project administration, V.S.; funding acquisition, V.S. and M.K. All authors have read and agreed to the published version of the manuscript.

Funding: This research was partially funded by the Health Pilot Research Project Training Program of the University of Cincinnati Education and Research Center, grant T42 OH008432-17, and by NSF through grant PFI-RP 2016484.

Data Availability Statement: The original contributions presented in the study are included in the article/Supplementary Materials, further inquiries can be directed to the corresponding author.

Acknowledgments: The authors express gratitude for the financial support from the National Institute for Occupational Safety and Health Pilot Research Project Training Program of the University of Cincinnati Education and Research Center (Grant no. T42 OH008432-17). M.K. extends gratitude to Melodie Fickenscher at the UC Advanced Materials Characterization Center for guidance and support through a Graduate Assistantship, as well as the Graduate Student Government (GSG) at UC for the Research Fellowship. V.S. acknowledges the financial support from the NSF through Grant PFI-RP 2016484.

Conflicts of Interest: The authors declare no conflicts of interest.

References

1. Zhang, Z.; Lee, C.-S.; Zhang, W. Vertically Aligned Graphene Nanosheet Arrays: Synthesis, Properties and Applications in Electrochemical Energy Conversion and Storage. *Adv. Energy Mater.* **2017**, *7*, 1700678. [CrossRef]
2. Wang, H.; Zhao, M.; Zhu, W.; Liu, Z.; Wang, G.; Tang, S.; Chen, D.; Lee, J.-M.; Yang, S.; Ding, G. High-performance humidity sensor constructed with vertically aligned graphene arrays on silicon schottky junctions. *Mater. Lett.* **2020**, *277*, 128343. [CrossRef]
3. Kundu, A.; Shetti, N.P.; Basu, S.; Mondal, K.; Sharma, A.; Aminabhavi, T.M. Versatile carbon nanofiber-based sensors. *Appl. Bio Mater.* **2022**, *5*, 4086–4102. [CrossRef] [PubMed]
4. Zhang, B.; Kang, F.; Tarascon, J.-M.; Kim, J.-K. Recent advances in electrospun carbon nanofibers and their application in electrochemical energy storage. *Prog. Mater. Sci.* **2016**, *76*, 319–380. [CrossRef]
5. Wu, H.; Zhou, Z.; Chen, L.; Li, W.; Han, Q.; Li, C.; Xu, Z.; Qian, X. PECVD-induced growing of diverse nanomaterials on carbon nanofibers under various conditions. *Mater. Lett.* **2018**, *216*, 291–294. [CrossRef]
6. Hussain, S.; Kovacevic, E.; Berndt, J.; Santhosh, N.M.; Pattyn, C.; Dias, A.; Strunskus, T.; Ammar, M.-R.; Jagodar, A.; Gaillard, M. Low-temperature low-power PECVD synthesis of vertically aligned graphene. *Nanotechnology* **2020**, *31*, 395604. [CrossRef]
7. Zhou, F.; Shan, J.; Cui, L.; Qi, Y.; Hu, J.; Zhang, Y.; Liu, Z. Direct Plasma-Enhanced-Chemical-Vapor-Deposition Syntheses of Vertically Oriented Graphene Films on Functional Insulating Substrates for Wide-Range Applications. *Adv. Funct. Mater.* **2022**, *32*, 2202026. [CrossRef]
8. Lin, Y.; Wei, H.; Leou, K.; Lin, H.; Tung, C.; Wei, M.; Lin, C.; Tsai, C. Experimental characterization of an inductively coupled acetylene/hydrogen plasma for carbon nanofiber synthesis. *J. Vac. Sci. Technol. B* **2006**, *24*, 97–103. [CrossRef]
9. Santhosh, N.M.; Filipič, G.; Tatarova, E.; Baranov, O.; Kondo, H.; Sekine, M.; Hori, M.; Ostrikov, K.; Cvelbar, U. Oriented carbon nanostructures by plasma processing: Recent advances and future challenges. *Micromachines* **2018**, *9*, 565. [CrossRef]
10. Conrads, H.; Schmidt, M. Plasma generation and plasma sources. *Plasma Sour. Sci. Technol.* **2000**, *9*, 441. [CrossRef]
11. Chen, J.; Bo, Z.; Lu, G. *Vertically-Oriented Graphene: PECVD Synthesis and Applications*; Springer: Cham, Switzerland, 2015; Volume 10.
12. Zhou, L.; Yang, Z.; Yang, J.; Wu, Y.; Wei, D. Facile syntheses of 3-dimension graphene aerogel and nanowalls with high specific surface areas. *Chem. Phys. Lett.* **2017**, *677*, 7–12. [CrossRef]
13. Dasgupta, K.; Khosravifar, M.; Sawant, S.; Adusei, P.K.; Kanakaraj, S.N.; Kasik, J.; Shanov, V. Nitrogen-Doped Flower-Like Hybrid Structure Based on Three-Dimensional Graphene. *Carbon* **2020**, *6*, 40. [CrossRef]
14. Zhao, J.; Shaygan, M.; Eckert, J.; Meyyappan, M.; Rümmeli, M.H. A Growth Mechanism for Free-Standing Vertical Graphene. *Nano Lett.* **2014**, *14*, 3064–3071. [CrossRef] [PubMed]
15. Seo, D.; Kumar, S.; Ostrikov, K. Control of morphology and electrical properties of self-organized graphenes in a plasma. *Carbon* **2011**, *49*, 4331–4339. [CrossRef]
16. Zheng, S.; Zhong, G.; Wu, X.; D'Arsiè, L.; Robertson, J. Metal-catalyst-free growth of graphene on insulating substrates by ammonia-assisted microwave plasma-enhanced chemical vapor deposition. *RSC Adv.* **2017**, *7*, 33185–33193. [CrossRef]
17. Kousar, A.; Pande, I.; Pascual, L.F.; Peltola, E.; Sainio, J.; Laurila, T. Modulating the Geometry of the Carbon Nanofiber Electrodes Provides Control over Dopamine Sensor Performance. *Anal. Chem.* **2022**, *95*, 2983–2991. [CrossRef]
18. Melechko, A.V.; Merkulov, V.I.; McKnight, T.E.; Guillorn, M.; Klein, K.L.; Lowndes, D.H.; Simpson, M.L. Vertically aligned carbon nanofibers and related structures: Controlled synthesis and directed assembly. *J. Appl. Phys.* **2005**, *97*, 041301. [CrossRef]
19. Zhang, H.; Wu, S.; Lu, Z.; Chen, X.; Chen, Q.; Gao, P.; Yu, T.; Peng, Z.; Ye, J. Efficient and controllable growth of vertically oriented graphene nanosheets by mesoplasma chemical vapor deposition. *Carbon* **2019**, *147*, 341–347. [CrossRef]
20. Wang, H.; Moore, J.J. Low temperature growth mechanisms of vertically aligned carbon nanofibers and nanotubes by radio frequency-plasma enhanced chemical vapor deposition. *Carbon* **2012**, *50*, 1235–1242. [CrossRef]

21. Khosravifar, M.; Dasgupta, K.; Kondapalli, V.K.R.; Fang, Y.; Alexander, R.; Shanov, V. Nitrogen-Doped, Vertically Aligned Structures of Graphene and Carbon Nanofibers for Energy Storage Applications. *Appl. Nano Mater.* **2024**, *7*, 10284–10292. [CrossRef]
22. Zhang, L.; DeArmond, D.; Alvarez, N.T.; Malik, R.; Oslin, N.; McConnell, C.; Adusei, P.K.; Hsieh, Y.-Y.; Shanov, V. Flexible Micro-Supercapacitor Based on Graphene with 3D Structure. *Small* **2017**, *13*, 1603114. [CrossRef] [PubMed]
23. Kondapalli, V.K.R.; Zhang, G.; Zhang, Y.; Khosravifar, M.; Brittingham, K.; Phan, N.; Yarmolenko, S.; Bahk, J.-H.; Shanov, V. New architecture of 3D graphene with enhanced properties obtained by cold rolling. *Carbon* **2023**, *207*, 116–128. [CrossRef]
24. Melechko, A.V.; Desikan, R.; McKnight, T.E.; Klein, K.L.; Rack, P.D. Synthesis of vertically aligned carbon nanofibres for interfacing with live systems. *J. Phys. D Appl. Phys.* **2009**, *42*, 193001. [CrossRef]
25. Jung, P.G.; Jung, I.D.; Lee, S.M.; Ko, J.S. Fabrication of self-encapsulated nickel microchannels and nickel nanowalls by reactive ion etching. *J. Mater. Process. Technol.* **2008**, *208*, 111–116. [CrossRef]
26. Dervishi, E.; Li, Z.; Shyaka, J.; Watanabe, F.; Biswas, A.; Umwungeri, J.L.; Courte, A.; Biris, A.R.; Kebdani, O.; Biris, A.S. The role of hydrocarbon concentration on the synthesis of large area few to multi-layer graphene structures. *Chem. Phys. Lett.* **2011**, *501*, 390–395. [CrossRef]
27. Saeed, M.; Alshammari, Y.; Majeed, S.A.; Al-Nasrallah, E. Chemical vapour deposition of graphene—Synthesis, characterisation, and applications: A review. *Molecules* **2020**, *25*, 3856. [CrossRef]
28. Gupta, R.; Sharma, S.C. Parametric Study of Plasma Characteristics and Carbon Nanofibers Growth in PECVD System: Numerical Modeling. *Plasma Chem. Plasma Process.* **2020**, *40*, 1331–1350. [CrossRef]
29. Collison, W.Z.; Ni, T.Q.; Barnes, M.S. Studies of the low-pressure inductively-coupled plasma etching for a larger area wafer using plasma modeling and Langmuir probe. *J. Vac. Sci. Technol. A Vac. Surf. Films* **1998**, *16*, 100–107. [CrossRef]
30. Vesel, A.; Zaplotnik, R.; Primc, G.; Mozetič, M. A review of strategies for the synthesis of N-doped graphene-like materials. *Nanomaterials* **2020**, *10*, 2286. [CrossRef]
31. Inagaki, M.; Toyoda, M.; Soneda, Y.; Morishita, T. Nitrogen-doped carbon materials. *Carbon* **2018**, *132*, 104–140. [CrossRef]
32. Das, A.; Chakraborty, B.; Sood, A.K. Raman spectroscopy of graphene on different substrates and influence of defects. *Bull. Mater. Sci.* **2008**, *31*, 579–584. [CrossRef]
33. Zafar, Z.; Ni, Z.H.; Wu, X.; Shi, Z.X.; Nan, H.Y.; Bai, J.; Sun, L.T. Evolution of Raman spectra in nitrogen doped graphene. *Carbon* **2013**, *61*, 57–62. [CrossRef]
34. Dangel, G.R.; Kumakli, H.; Rahm, C.E.; White, R.; Alvarez, N.T. Nanoelectrode ensembles consisting of carbon nanotubes. *Appl. Sci.* **2021**, *11*, 8399. [CrossRef]
35. Brownson, D.A.; Ferrari, A.G.-M.; Ghosh, S.; Kamruddin, M.; Iniesta, J.; Banks, C.E. Electrochemical properties of vertically aligned graphenes: Tailoring heterogeneous electron transfer through manipulation of the carbon microstructure. *Nanoscale Adv.* **2020**, *2*, 5319–5328. [CrossRef]
36. Ji, Q.; Hu, C.; Liu, H.; Qu, J. Development of nitrogen-doped carbon for selective metal ion capture. *Chem. Eng. J.* **2018**, *350*, 608–615. [CrossRef]
37. World Health Organization. Lead in Drinking-Water: Health Risks, Monitoring and Corrective Actions: Technical Brief. Available online: https://iris.who.int/bitstream/handle/10665/361821/9789240020863-eng.pdf (accessed on 1 January 2022).